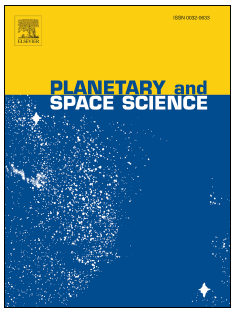

Calibration of NOMAD on ExoMars Trace Gas Orbiter: Part 3 - LNO validation and instrument stability

G. Cruz Mermy, F. Schmidt, I.R. Thomas, F. Daerden, B. Ristic, M.R. Patel, J.-J. Lopez-Moreno, G. Bellucci, A.C. Vandaele, the NOMAD Team

PII: S0032-0633(21)00238-5

DOI: https://doi.org/10.1016/j.pss.2021.105399

Reference: PSS 105399

To appear in: *Planetary and Space Science*

Received Date: 19 July 2021

Revised Date: 8 December 2021

Accepted Date: 9 December 2021

Please cite this article as: Mermy, G.C., Schmidt, F., Thomas, I.R., Daerden, F., Ristic, B., Patel, M.R., Lopez-Moreno, J.-J., Bellucci, G., Vandaele, A.C., the NOMAD Team, Calibration of NOMAD on ExoMars Trace Gas Orbiter: Part 3 - LNO validation and instrument stability, *Planetary and Space Science* (2022), doi: https://doi.org/10.1016/j.pss.2021.105399.

Calibration of NOMAD on ExoMars Trace Gas Orbiter: Part 3 - LNO validation and instrument stability

G. Cruz Mermy[1], F. Schmidt[1,2], I. R. Thomas[3], F. Daerden[3], B. Ristic[3], M. R. Patel[4,5], J.-J. Lopez-Moreno[6],G. Bellucci[7], A.C. Vandaele[3] and the NOMAD Team

[1]Université Paris Saclay, Géosciences Paris Saclay (GEOPS), 91405 Orsay, France

[2]Institut Universitaire de France (IUF)

[3]Royal Belgian Institute for Space Aeronomy (BIRA-IASB), Av. Circulaire 3, 1180 Brussels, Belgium

[4]The Open University, Walton Hall, Milton Keynes, MK7 6AA, U.K.

[5]STFC Rutherford Appleton Laboratory, Oxfordshire OX11 0QX, U.K

[6]Instituto de Astrofisica de Andalucia (IAA/CSIC), Granada, Spain

[7]Istituto di Astrofisica e Planetologia Spaziali (IAPS/INAF), Via del Fosso del Cavaliere, 00133 Rome, Italy

*corresponding author: guillaume.cruz-mermy@universite-paris-saclay.fr

Keywords. Space instrumentation; calibration; Mars; spectroscopy; surface; ExoMars

1. Introduction

The ExoMars program consists of two missions designed to study the trace gases of the martian atmosphere but also to acquire information on potential ongoing geological and biological processes on the surface of Mars (Vago et al., 2015). Since April 2018, the four instruments aboard the ESA/Roscosmos ExoMars Trace Gas Orbiter mission has acquired observations of both the

atmosphere and surface of Mars. Among them the NOMAD instrument (Nadir and Occultation for MArs Discover), led by the Belgian Institute for Space Aeronomy (BIRA-IASB), is a suite of three spectrometers spanning the UV and IR spectral range: SO (Solar occultation), LNO (limb, nadir, and occultation) and UVIS (ultraviolet-visible). The three channels work separately but are all controlled via a single main electronic interface (Neefs et al., 2015). The two first channels are infrared spectrometers based upon the SOIR (Solar Occultation in the InfraRed) instrument aboard the Venus Express mission (Nevejans et al., 2006).

The LNO channel is a compact high-resolution echelle grating spectrometer with an acousto-optic tunable filter (AOTF) working in the infrared domain from 2.3 μm to 3.8 μm (4250-2630 cm^{-1}) with a resolving power ($\lambda/\Delta\lambda$) of around 10000, specially designed for nadir observation. With such high resolving power combined with the near-circular orbit of TGO permitting 12 orbits in one sol, promoting a global coverage of the planet, the NOMAD-LNO instrument is perfectly suited to study the martian surface and atmosphere.

The main objective of this article is to propose an original calibration procedure, adaptable for the full dataset of NOMAD-LNO. This calibration is complementary to the one proposed by Thomas et al. (2021) who developed a fully empricial method using in-flight data. In their paper the LNO ground calibration, occultation and nadir boresight pointing vectors, detector characterisation and illumination pattern are covered. A combination of several observation of the sun is used to derive instrument temperature effects such as the shape and intensity of a LNO spectrum. The radiometric calibration is done by assuming temporal stability of the instrument and directly using solar observation to calibrate nadir observation.

In this paper we will not assume temporal stability of the instrument. Our approach is thus able to investigate the temporal evolution of the instrumental sensitivity, which is expected to vary due to degradation by energetic particles. This approach will be based on an empirical continuum removal to take into account the departure between actual blaze function and its theoretical form. By construction, our approach is thus more robust but may fail to model some instrumental effect such as the temperature dependence of the blaze and AOTF transfer function on the raw continuum of an LNO spectrum. The main calibration of NOMAD-LNO is well described in

Thomas et al. (2021). This complementary work aims to validate the calibration of LNO but also to give additional information about instrumental transfer function and instrumental line shape.

2. NOMAD LNO instrument

The optical design of the LNO spectrometer is identical to that of SO and therefore very similar to SOIR (Nevejans et al., 2006; Vandaele et al., 2013), it is a combination of a high-dispersion echelle grating along with an AOTF and a cooled detector. The main advantage of using an echelle grating is that the full height of the detector can be used to register spectral lines (Neefs et al., 2015), which greatly improves the SNR after column binning. In the spatial direction, the detector contains 256 rows of pixels and only 144 of the 150 illuminated spatial lines are read out (Thomas et al., 2021). The AOTF is placed as diffraction order sorting devices in front of the spectrometer section to avoid order overlap at the output of the grating (Neefs et al., 2015). More information regarding the LNO channel, its working principle, and technical details can be found in previous articles (Neefs et al., 2015; Thomas et al., 2016, 2021).

Before starting a nadir observation, the detector needs to be cooled to its operating temperature of approximately 90 K (Neefs et al., 2015) to ensure that the thermal noise of the environment is not measured by the spectrometer. The AOTF will select the diffraction order to be observed, therefore, three types of observations are possible :

- Miniscan: Only a fraction of the entire spectral range is measured. The AOTF frequency slowly varies to observe the signal across a few diffraction orders and the transition between them.

- Fullscan: The entire spectral range of the channel is measured. The AOTF input varies by large steps, covering one diffraction order at a time.

- Dedicated scan: special AOTF frequencies are observed to select the corresponding diffraction order (for instance only the one where methane absorption bands are present).

As well as the SO channel, LNO can operate looking toward the sun which allows measurement of the solar lines for precise in-flight calibration. The solar miniscans and fullscans are precious

observation that provides complementary information on the instruments. Solar miniscans allow a precise determination of the AOTF transfer function shape and the Instrument Line Shape but each miniscan covers only a limited spectral range. A first in-flight calibration using miniscans has been proposed by Liuzzi et al. (2019). Fullscans are dedicated to spectral and photometric calibration as the whole spectral range is covered. In this work, the calibration model built for LNO is based on the solar fullscans observations.

3. Data

3.1. Solar fullscan

The NOMAD-LNO fullscans are solar observation made for calibration purposes. The instrument, normally in nadir position, is pointing toward the sun. The choice of using solar fullscans was made for two reasons. First, there are not enough miniscans to cover all diffraction orders with a significant amount of data while fullscans always cover the whole spectral range which allows testing the time dependence of the calibration. Second, it is important to estimate the instrumental sensitivity over the whole diffraction order range. As of June 2020, six solar calibrations have been performed on the following dates: 02/07/2018, 01/11/2018, 14/03/2019, 09/06/2019, 07/12/2019 and 05/01/2020. A typical fullscan observation is shown in figure 1. The x-axis is the pixel number (sometimes also called spectel), the y-axis is the diffraction order (i.e. the AOTF frequency) and the contours shows the sensitivity of the detector to incoming solar radiation (in ADU for Analog to Digital Units). As a function of the pixel number, the sensitivity is best between 100 and 250 and very low between 1 and 100. This shape is related to the Blaze function as it reaches lower values on the edge of the detector (pixel number 1 and 320). As a function of the diffraction order, the sensitivity is good around order 130 and best between order 160 and 200. This is related to the scientific goal of NOMAD, as it was designed to study the atmosphere (CO, CO_2, and H_2O between orders 163 and 192) and its traces gases (CH_4 between orders 130-136). Raw data (in ADU) are already dark subtracted directly onboard. Before using the fullscans as raw data for the calibration, a normalization needs to be done to account for the integration time t_{int}, the spectral resolution Δ_ν (varying across the spectral range), the number of accumulation NOA of recorded spectra, and the binning bin done before transmitting the data to Earth. The

normalization equation follows :

$$S_{obs} = \frac{Counts(ADU)}{t_{int}.\Delta_{\nu}.NOA.bin} \quad (1)$$

Where Counts is the dark-subtracted raw spectrum across the 320 spectels. For the LNO fullscan, instrument parameters are:

- $t_{int} = 2$ ms
- $0.1469 \leq \Delta_{\nu} \leq 0.2649\ cm^{-1}$ between order 110 and 215 (Liuzzi et al., 2019)
- $NOA = 78$
- $bin = 24$ as the 24 central lines are illuminated by the sun and stacked to increase the signal for the calibration

These parameters are constant for all LNO fullscans. The spectrum S_{obs} is considered the actual observation of the sun. Each sequence of a fullscan starts with the order 110 and ends with the order 215. This sequence is then repeated several times (between 14 and 34 times). Due to the very weak signal-to-noise ratio on the edge of the detector (spectels 1 to 50) only spectels 50 to 320 are considered for the calibration.

3.2. Construction of a reference synthetic solar spectrum for NOMAD

The sun is the best blackbody available for in-flight calibration because its spectrum is well defined and its time variations are minimal. The synthetic solar spectrum that we use to compare LNO solar observations is derived from the Fourier Atmospheric Chemistry Experiment (ACE) spectrometer data aboard SciSat-1, operating in the spectral range 2-13 μm (750 - 4430 cm^{-1}) at a very high spectral resolution (0.02 cm^{-1}) (Hase et al., 2010). The processed data available is a transmittance solar spectrum (called S_T hereafter) which was converted to spectral irradiance spectrum (in $W.cm^{-2}.(cm^{-1})^{-1}$) with a fit of the spectral continuum of the *NewKurucz* (Chance and Kurucz, 2010) solar spectrum S_{Kurucz} from the MODTRAN spectral database. To do so we first defined the continuum by a convolution with a median Gaussian filter $G(0)$ with a large standard deviation (σ) to avoid the contribution of solar lines:

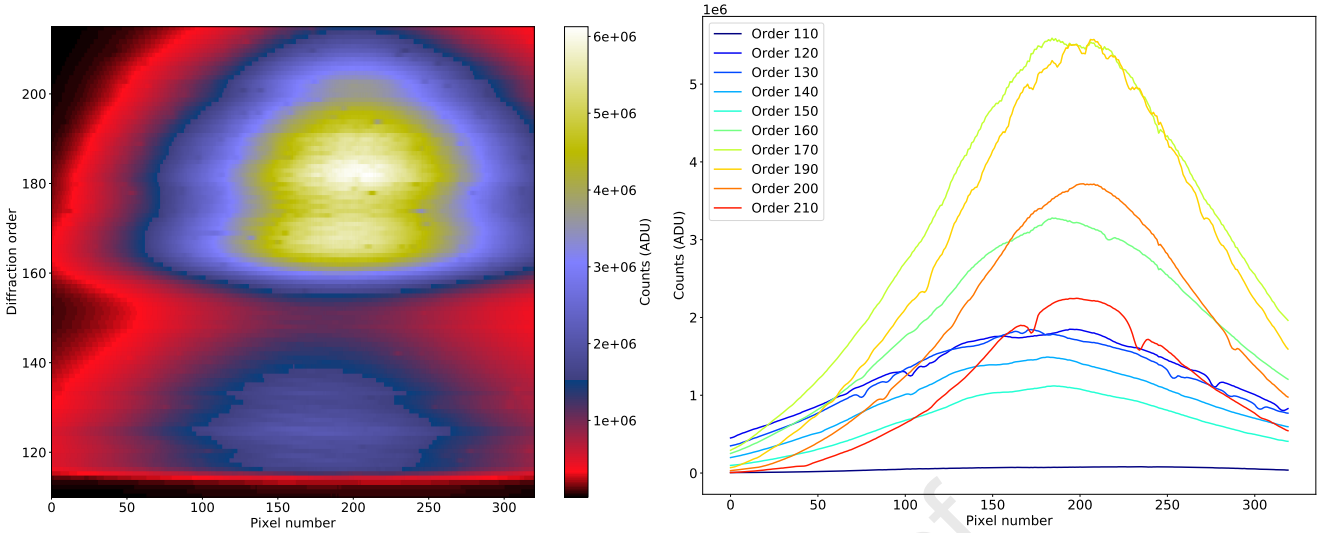

Figure 1: Example of a typical NOMAD-LNO solar fullscan (observation of 14/03/2019, sequence number 10 out of 15). Here the 24 central lines illuminated are summed to promote a better SNR. The left figure shows the complete fullscan across the whole LNO spectral range (order 110 to 215). Each line of the image represents a spectrum at a particular diffraction order sampled on the 320 spectral spectels of the detector (i.e the wavenumbers). The colors represent the intensity (expressed in ADU) measured by the detector and solar lines are visible as spots. The right figure shows a cross-section within the fullscan at particular diffraction orders. Here the characteristic "bell" shape of the continuum is clearly visible, the width and height of each spectrum is order-dependent and are related to the instrument-specific design (AOTF + blazed grating). Weak solar lines are also visible which illustrates the high spectral resolution of the instrument.

$$S_{continuum} = S_{Kurucz} \star \mathcal{G}(0, \sigma) \tag{2}$$

Then, the solar continuum $S_{continuum}$ was interpolated in the wavenumbers sampling of the ACE spectrum to maintain the very high spectral resolution. The spectrum is then converted to spectral radiance (in $W.cm^{-2}.(cm^{-1})^{-1}.sr^{-1}$) by dividing the interpolated $S_{continuum}$ spectrum by the solid angle (in sr units) with which the sun is observed by LNO. In this case the sun is entirely resolved by the detector therefore the solid angle is simply the surface of the sun divided by the square of the Mars-Sun distance (in km). Here we considered the mean Mars-Sun distance (1.524 AU). We also integrate the Mars-Sun distance ($d_{\odot\sigma^{\prime}}$ (in AU) in $S_{continuum}$ since the *NewKurucz* solar spectrum was measured from Earth orbit at a distance of 1 AU. This leads to the final spectrum S_L:

$$S_L = S_{continuum}.S_T/d^2_{\odot\sigma^{\prime}} \tag{3}$$

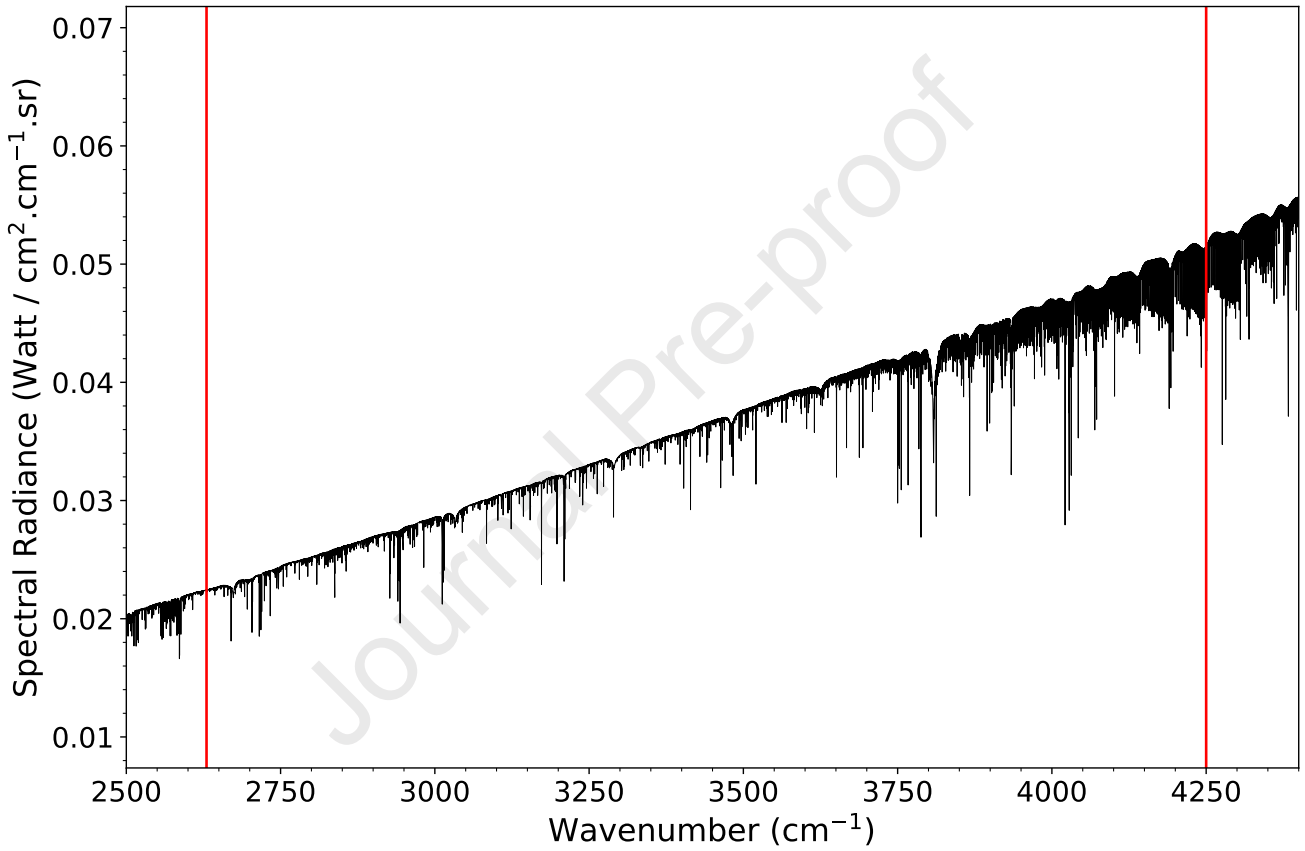

Figure 2: Solar spectrum (S_L) used in this study in spectral radiance and the mean distance Mars-Sun (1.524 AU). The very high spectral resolution of the Fourier ACE spectrometer allows the identification of weak solar lines, which is necessary for the calibration of LNO. The LNO spectral range is shown as red vertical lines.

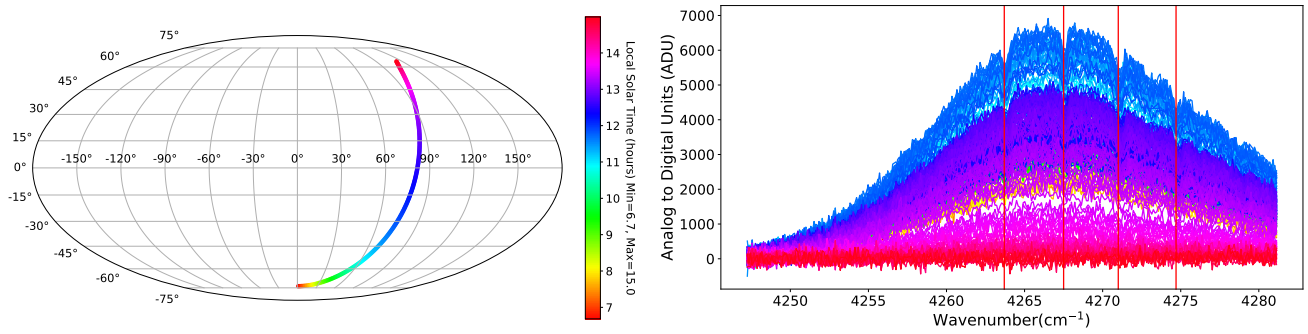

Figure 3: Order 189: groundtrack (left) and raw spectra (right) of 18/09/2018, the colors refer to local solar time. The low-altitude near-circular orbit of TGO allows observations at various local times. The characteristic 'bell" shape of LNO spectra is visible, especially when the signal is strong at noon local solar time (in blue). The atmospheric bands are also visible, here red vertical lines indicate the CO absorption bands.

3.3. NOMAD-LNO observation (nadir)

The science phase of the LNO channel started in March 2018. During one orbit (nadir-looking), one to six diffraction orders can be measured, for instance when 3 orders are measured the observation cycle lasts 15 seconds and is decomposed into 3 periods of 5 seconds corresponding to a different configuration of the AOTF (Vandaele et al., 2015, 2018). Thus, for the same cycle, three diffraction orders can be measured, each measurement is completed by a measurement of the "Dark" which is then subtracted directly on board (Vandaele et al., 2018). In April 2021, more than 12,810 files are available, each file corresponds to a particular diffraction order during one orbit. Not all diffraction orders are measured in each orbit and most of the time a combination of useful orders for a science objective are acquired together, such as orders 131-136 (CH_4), 146-150 (CO_2), 167-171 (H_2O), and 186-192 (CO) (Liuzzi et al., 2019; Vandaele et al., 2019). We decide here to illustrate our calibration with order 189 due to the significant amount of data and for its scientific interest (Smith, 2021). Thus, for a particular order, the time necessary to obtain a global map coverage of the planet can be spread over a long time, typically one martian year. To exclude any temporal variation in the instrument that could bias the calibration and the reflectance map produced, it is important to test the time dependence of the instrument on the photometric sensitivity to look at the potential aging of the detector before calibrating data spanning several years. A typical LNO orbit is shown in figure 3 for order 189.

4. Method

The calibration aim was to build a model to estimate the spectral conversion (wavenumbers in cm^{-1} for each spectels of the detector) and the photometric sensitivity (conversion factor from ADU to spectral radiance). The model must be versatile enough to face the uncertainties of some instrumental functions, such as the AOTF transfer function and the grating blaze function.

The method used here is based on the usual comparison between a real solar observation and a simulated solar spectrum. The observations are LNO solar fullscans and we aim to simulate the same observation by accounting for the AOTF and grating effects. The comparison is done after spectra continuum correction to work out the baseline uncertainties. This approach is of particular importance for correct calibration of nadir data, for which there is no observation free of atmospheric absorption (Liuzzi et al., 2019). The calibration steps we perform are the following :

1. First-order spectral calibration: conversion of detector spectel number and diffraction order to wavenumber (Section 4.1)
2. Calibration inversion, by minimizing the residual between observation and simulation, following these steps:
   (a) Application of the grating blaze function and AOTF transfer function shape (Section 4.2.1)
   (b) Simulation of the Instrument Line Shape (ILS) (Section 4.2.2)
   (c) Integration of a residual wavenumber shift (Section 4.2.3)
   (d) Continuum removal to remove the shape imposed by the instrumental functions (Section 4.2.4)
   (e) Normalization and estimation of the sensitivity (Section 4.2.5)
   (f) Computation of the residue (Section 4.3)
3. By construction, the result of the minimization leads to the estimation of the instrumental sensitivity

An illustration of the calibration pipeline with the different corresponding sections is given figure 4.

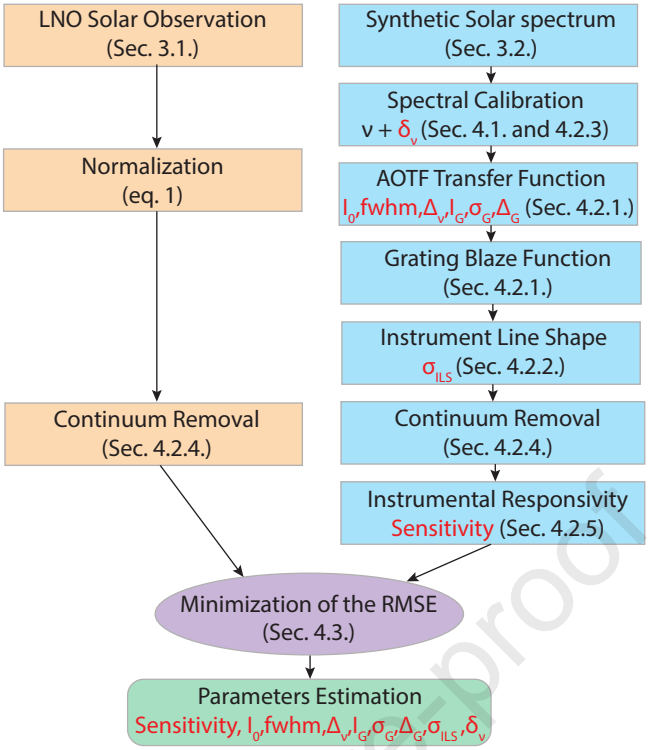

Figure 4: Flowchart summarizing the steps of the calibration model. The parameters estimated by the inversion are indicated in red.

4.1. Spectral calibration

The very first step to perform is to compute the spectral calibration which is based on the position of well-defined solar lines in the calibration spectra that can be used to match a line's frequency with the spectel number in which it falls (Liuzzi et al., 2019). The diffraction order number is related to the AOTF frequency and the aim is to get a relationship between the spectel number of the detector and the wavenumber, at a corresponding diffraction order. This relationship is modeled by a second-order polynomial :

$$\frac{\nu}{m} = F_0 + F_1.p + F_2.p^2 \tag{4}$$

Where ν is the wavenumber, m is the diffraction order and p is the spectel number (from 1 to 320). The coefficients F_0, F_1 and F_2 were obtained by Liuzzi et al. (2019) using Miniscan acquisitions and a total of 70 solar lines. The central spectel wavenumber of the considered order is noted ν_0 for spectel 160. The Free Spectral Range (FSR) is the wavelength range in which there is no overlap by adjacent orders. It can be computed using equation 4 at the spectel 160

(center of the detector) and gives a value of 22.545 cm^{-1} which is very close to what is reported in Neefs et al. (2015) with a value of 22.56 cm^{-1}. The FSR is expected to be a constant for echelle gratings (Neefs et al., 2015). To take into account small residual wavenumber shift, we introduced a parametrization described in section 4.2.3.

4.2. Photometric calibration

To simulate the instrumental effects, we need to take into account the instrumental transfer function T (here due to the grating and the AOTF), and the instrumental line shape ILS that blurred the signal in spectral domain. A simplified expression of the instrumental effects is:

$$S_{sim}(\nu) = (S_L(\nu).T(\nu)) \star ILS \tag{5}$$

Where $S_L(\nu)$ is the simulated solar spectrum described in section 3.2 and $T(\nu)$ is the instrumental transfer functions described hereafter. In the next sections, we will describe precisely the instrument model taken into account. We will emphasize for all functions the main parameter ν (representing the wavenumber) and the unknown parameters that our inversion scheme will estimate.

4.2.1. Instrumental transfer function

Grating blaze function. A diffraction grating or echelle spectrometer is an optical device which allows diffraction of the incident light into different diffraction orders. Slit spacing controls the extent of the diffraction for a given wavelength. For the LNO spectrometer, a "blazed grating" is used where the grooves are tilted in a special angle, called the "Blaze angle". This angle is generally chosen to optimize the efficiency of the diffraction for a given wavelength. The commonly adopted geometry is called "Littrow configuration" in which the Blaze angle is chosen so that the incident and diffraction angle are the same, and are equal to the Blaze angle. Moreover, the LNO has a near-Littrow configuration (Neefs et al., 2015) to slightly separate the incident beam from the diffracted beam. Thus, the grating is tilted so that both beams make a small γ angle between the perpendicular plane to the grating surface and the grooves. It is also necessary to take into account a slight deviation angle i of the incident angle with respect to the Blaze angle in the perpendicular plane to the grooves. The grating equation becomes (Neefs et al., 2015):

Parameters	Value	Precision	Unit
Blaze angle θ_B	63.43	± 0.1	$^\circ$
Groove density σ (at 0°C)	4.033512		lines/mm
Number of grooves N	≥ 765		
Groove spacing d	248.06	± 0.001	μm
Off-Littrow angle γ	2.75	± 0.0025	$^\circ$
Off-Blaze angle i	0	± 0.016	$^\circ$

Table 1: Grating characteristics of the LNO channel, from Neefs et al. (2015).

$$\frac{m}{\nu} = \frac{(\cos\alpha + \sin\beta).\cos i.\cos\gamma}{\sigma} = \frac{2\sin\theta_B.\cos i.\cos\gamma}{\sigma} \tag{6}$$

Where m is the diffraction order, α is the incident angle, β is the diffraction angle, θ_B is the Blaze angle, σ is the grating groove density (lines/mm), and ν is the wavenumber. The blaze grating characteristics of the LNO channel are summarized in table 1. The grating efficiency is estimated at 85% in the center of the grating and falls to 40% at the edges (Neefs et al., 2015). For each wavenumber within each order, we compute the diffraction angle β using equation 6. Then, we estimate the blazing efficiency for which we adopt the following relation :

$$T_{Blaze}(\nu) = C.\left[\mathrm{sinc}(\nu.\frac{\sigma.\cos\gamma.\cos\alpha}{\cos\alpha_B}.(\sin\alpha_B + \sin(\beta - \theta_B)))\right]^2 \tag{7}$$

Where $\alpha_B = \theta_B - \alpha$, the angle between the incident beam and the normal of the facet in the perpendicular plane to the grooves, and the grating geometric parameters $C = 1$ if $\alpha > \beta$ or $\left(\frac{\cos\beta}{\cos\alpha}\right)^2$if $\alpha < \beta$. The measured global shape of NOMAD spectra is partly determined by this $T_{Blaze}(\nu)$ function.

The LNO grating is made of an aluminum alloy (Neefs et al., 2015) and is therefore subject to compressions/expansions due to temperature changes. This would lead to groove density variations and shift the position of the function on the detector spectels. If the temperature within the spectrometer is known, then this effect can be taken into account considering the following formula describing the groove length σ. From a known groove length σ_1 at temperature T_1 it is possible to estimate the groove length σ_2 at temperature T_2 using the thermal expansion equation (Marquardt et al., 2000):

a	$-4.1272.10^{-3}$
b	$-3.0640.10^{-6}$
c	$8.7960.10^{-8}$
d	$1.0055.10^{-10}$
T_1	$24.5°C$
σ_1	248.06µm

Table 2: Reference groove spacing and temperature for the LNO channel from Marquardt et al. (2000).

$$\sigma_2 = \sigma_1.\frac{(1+(a+b.T_2+c.T_2^2+d.T_2^3))}{(1+(a+b.T_1+c.T_1^2+d.T_1^3))} \tag{8}$$

Where a, b, c and d are instrument-specific coefficients for the LNO channels, T_2 is the given instrument temperature, T_1 is the design temperature and σ_1 is the reference groove spacing at design temperature (see table 1). Table 2 summarizes their value. Because the blaze function mainly controls the position of a NOMAD raw spectrum on the 320 pixels, especially the position of maximum intensity, and since the temperature of the grating is not perfectly known, our strategy was to perform a rough estimation: we average all data from the same fullscan for each order and perform a regression to estimate the temperature to use for each order. The residual discrepancies between blaze function and real data are removed by continuum removal.

AOTF transfer function shape. The AOTF is an electro-optical device based on the Bragg diffraction, the interaction between acoustic and electromagnetic waves, in a birefringent crystal of Tellurium dioxide (TeO_2). Under the application of a radio-frequency (using a Transducer) the crystal vibrates and its internal structure is alternatively compressed and dilated through the crossing of the oscillating acoustic wavefront. This results in a periodic modification of its optical properties, its refractive index, thus producing diffraction of the incident light. The intensity of the diffraction is proportional to the amplitude of the acoustic signal applied to the crystal. In addition, changing the acoustic frequency applied to the crystal alters the periodicity of the refractive index variation and therefore the wavelength at which the light is diffracted. The AOTF crystal acts mainly as a filter for selecting the desired order of diffraction which will be transmitted to the diffraction grating. Thus, if no radiofrequency is applied to the crystal (AOTF off) then the spectrometer measures the thermal noise and the background noise also called "dark observation" which are used

to correct the specific noises of the detector environment. The main characteristics of the AOTF used for the LNO channel are well described in Neefs et al. (2015). The AOTF transfer function shape is usually modeled by a sinc-square function. However, several tests showed that this model does not accurately represent the NOMAD-LNO AOTF (Liuzzi et al., 2019). This may be due to the contributions from adjacent orders which are not negligible and can be related to two main reasons :

- The AOTF input radiofrequency is not centered on the AOTF transfer function with respect to the observed order, so the AOTF admits throughput of adjacent orders.
- The Free Spectral Range of the grating is smaller than the detector's sensitive area causing invasion from adjacent orders.

To properly account for this effect, we tested several models that would increase the contribution from adjacent orders in the AOTF transfer function shape (using multiple sinc-square, using one sinc-square per order or adding a linear function to add a background contribution). The most promising model turns out to be the use of a Gaussian function along with the usual sinc-square function which is similar to what is reported in Liuzzi et al. (2019). The AOTF transfer function shape follows :

$$T_{sinc}(\nu, I_0, fwhm, \Delta_\nu) = I_0 . \left[\mathrm{sinc}\left(0.886 . \frac{\nu - \nu_0 - \Delta_\nu}{fwhm}\right)\right]^2 \tag{9}$$

$$T_{gauss}(\nu, I_G, \sigma_G, \Delta_G) = I_G . \exp\left[\frac{(\nu - \nu_0 - \Delta_G)^2}{\sigma_G^2}\right] \tag{10}$$

$$T_{AOTF}(\nu, I_0, fwhm, \Delta_\nu, I_G, \sigma_G, \Delta_G) = T_{sinc} + T_{gauss} \tag{11}$$

Where $fwhm$ is the full width at half maximum of the sinc-square function, Δ_ν is the sinc-square shift in wavenumber from the central wavenumber of the considered order ν_0, I_0 the sinc-square amplitude, I_G the Gaussian amplitude, σ_G the Gaussian standard deviation and Δ_G the shift in wavenumber of the Gaussian function. These are the six free parameters to estimate related to the AOTF. Adding a Gaussian function lowers the contribution of the transfer function side lobes,

which were related to the sinc-square function, but widens the shape of the main lobe and prevents the function to reach zero intensity between the main lobe and the first side lobe. This allows the increase of the contribution from the first nearby order. The main lobe is still centered on the central order which guarantees that most of the filtered signal is related to this order.

Final expression. The simulated solar spectrum is therefore constrained by the shape and intensity of the AOTF transfer function and the grating blaze function. The contribution from one order depends on the product of both functions at one particular wavenumber (i.e., on a spectel number). Contribution from adjacent orders is summed on the 320 spectral detector spectels which samples the wavenumber of the central order. The expression of a simulated solar observation by LNO is shown in equation 12.

$$S_{sim}^{instru}(\nu, I_0, fwhm, \Delta_\nu, I_G, \sigma_G, \Delta_G) = \sum_{m-\Delta m}^{m+\Delta m} S_L.(T_{Blaze}.T_{AOTF}) \tag{12}$$

The calibration proposed here was made considering 3 adjacent orders ($\Delta m = 3$) following the work of Liuzzi et al. (2019) who has shown that using 3 adjacent orders amounts to considering more than 99% of the total flux for the LNO channel. The absolute amplitude of the blaze and AOTF transmittance are estimated jointly as a general instrument sensitivity (see section 4.2.5). T_{Blaze} and T_{AOTF} are usually normalized.

4.2.2. Instrument Line Shape (ILS)

The simulated solar spectrum (S_{sim}^{instru}) is first convolved to the Instrumental Line Shape (ILS), modeled here by a centered Gaussian function $\mathcal{G}(0, \sigma_\nu)$ defined by a standard deviation (σ_ν) similar to what is reported in Liuzzi et al., 2019 (Liuzzi et al., 2019). This result in a smoothed spectrum S_{sim}^{smooth} defined as:

$$S_{sim}^{smooth}(\nu, \sigma_\nu) = S_{sim}^{instru}(\nu) \star \mathcal{G}(0, \sigma_\nu) \tag{13}$$

This step is crucial to simulated realistic solar lines shape and to characterize the actual wavenumber resolution of the instrument. Also, as the initial solar spectrum (S_L) used for the calibration has a much higher spectral resolution than NOMAD, the convolution allows the simulated

spectrum to match the theoretical spectral resolution of the observation. To compute the spectral resolution as a function of the diffraction order, we first compute the AOTF driver frequency to AOTF central wavenumber following the tuning relation :

$$\nu_0 = G_0 + A.G_1 + A^2.G_2 \tag{14}$$

where ν_0 is the central wavenumber and A is the AOTF frequency. The coefficients G_0, G_1 , and G_2 were determined by Liuzzi et al. (2019) using miniscans. Then, we compute the spectral resolution at the desired diffraction order :

$$sr = sr_0 + \nu_0.sr_1 + \nu_0^2.sr_2 \tag{15}$$

The coefficients sr_0, sr_1 and sr_2 are empirical values obtained by Liuzzi et al. (2019) using miniscans. The spectral resolution is order-dependent and is estimated with the central wavenumber (ν_0) of each order. This value is used as initialization and we treat σ_ν as a free parameter.

4.2.3. Residual wavenumber shift

The spectral calibration (see section 4.1) is not perfectly constant over time and solar lines are slightly shifted from one observation to another. Despite a first rough estimation of the temperature of the grating blaze function some residual shift may persist due to small variation of the blaze function within the same order. Since the temperature of the grating is not known such an effect must be taken into account for precise calibration. Our approach is to estimate the shift for each observation to possibly improve the formulation of eq. 4. We introduce a residual shift in wavenumber (δ_ν) between the observation (S_{obs}) and simulation (S_{sim}^{smooth}), the simulated spectra was resampled on the observed wavenumber with the linear resampling method:

$$S_{sim}^{smooth,resamp}(\nu) = S_{sim}^{smooth}(\nu + \delta_\nu) \tag{16}$$

with the wavenumber shift (δ_ν) set as a free parameter.

4.2.4. Continuum removal

The justification of this continuum removal step is done section 5. We propose to use the continuum estimation noted $\mathfrak{C}$, using the following approach :

$$S_{sim}^{smooth,resamp,flat}(\nu) = \frac{S_{sim}^{smooth,resamp}(\nu)}{\mathfrak{C}(S_{sim}^{smooth,resamp}(\nu))}.\overline{S_L} \tag{17}$$

$$S_{obs}^{flat}(\nu) = \frac{S_{obs}(\nu)}{\mathfrak{C}(S_{obs}(\nu))}.\overline{(S_{obs})} \tag{18}$$

Where $\overline{S_L}$ is the mean solar radiance taken from the input solar spectrum at the desired order and $\overline{(S_{obs})}$ is the mean of the normalized observation recorded by the detector for the desired order and sequence. Both means are computed with spectels 50 to 320. We used the function $\mathfrak{C}$ following the Asymmetric Least Squares smoothing (Eilers et al., 2005) with the following parameters:

- Smoothness $\lambda = 1.10^2$;
- Asymmetry $p = 0.99$;
- Number of iterations : 10 ;

4.2.5. Sensitivity

The sensitivity of the instrument is computed using the following equation :

$$Sensitivity = \frac{\left\| \overline{S_{sim}^{smooth,resamp,flat}}(W.cm^{-2}.(cm^{-1})^{-1}.sr^{-1}) \right\|}{\left\| \overline{S_{obs}^{flat}}(ADU.(cm^{-1})^{-1}.s^{-1}) \right\|} \tag{19}$$

Where $\overline{S_{obs}^{flat}}$ is the mean of the normalized observation after continuum correction as stated in equation 18 and $\overline{S_{sim}^{smooth,resamp,flat}}$ the mean of simulated spectra after the continuum correction. The two means are estimated for spectels 50 to 320. We choose to take the mean instead of the intensity at the center of the detector because it is a more robust indicator than the value of a single spectel which is subject to noise. The sensitivity simply expresses the mean radiance per counts per second of the 270 considered spectels. Once the sensitivity is known, the observation data can be calibrated into spectral radiance following:

$$S_{obs}^{flat,cal}(W.cm^{-2}.(cm^{-1})^{-1}.sr^{-1}) = Sensitivity.S_{obs}^{flat}(ADU.(cm^{-1})^{-1}.s^{-1}) \tag{20}$$

With S_{obs}^{flat} the normalized observation after continuum correction.

4.3. Calibration inversion

The aim is to retrieve the best parameters to simulate S_{sim} for each spectrum of each sequence of all solar fullscan. The goal is to compute the sensitivity (photometric calibration) but also to look at the potential correlation between the estimated free parameters and instrumental parameters such as temperature.

Since the AOTF parameters, the wavenumber shift, and the actual wavenumber resolution are not known and subject to change from one observation to another, we decided to estimate them by a fitting procedure. Except for the Gaussian and sinc-square functions intensities (the sum of which must be equal to 1, such that a filter is defined) all six other parameters are expressed in wavenumbers units (cm^{-1}) which makes it possible to assume the range in which we expect these parameters to fall. This is why we choose a bound-constrained minimization with the L-BFGS-B algorithm (Byrd et al., 1995; Zhu et al., 1997). The minimization equation follows:

$$\min_{I_0,fwhm,\Delta_\nu,I_G,\sigma_G,\Delta_G,\delta_\nu,\sigma_{ILS}} \left(\left\| S_{sim}^{smooth,resamp,flat}(I_0, fwhm, \Delta_\nu, I_G, \sigma_G, \Delta_G, \delta_\nu, \sigma_{ILS}) - S_{obs}^{flat,cal} \right\| \right) \quad (21)$$

The remaining residue between the spectra is estimated with the Root Mean Square Error (RMSE):

$$RMSE = \sqrt{\frac{\sum \left(S_{sim}^{smooth,resamp,flat} - S_{obs}^{flat,cal} \right)^2}{N}} \quad (22)$$

With N, the number of considered spectels, here 270 as the first 50 spectels are removed due to low SNR. The relative RMSE (rel_{RMSE}) can be defined as follow :

$$rel_{RMSE} = \frac{RMSE}{\overline{S_{sim}^{smooth,resamp,flat}}} \quad (23)$$

with $\overline{S_{sim}^{smooth,resamp,flat}}$, the mean of the simulation spectra. This gives the relative error (in %) between the observation and the simulation. The inversion stops when the norm of the projected gradient of the RMSE is less or equal to 10^{-8} with a step size of 10^{-5} for each parameter.

A total of 8 free parameters were retrieved for each spectrum of all sequences and all fullscans.

Parameter	Initialization	Range	Units
I_0	0.5	0.1 - 1.0	
fwhm	18	12.0 - 20.0	cm^{-1}
Δ_ν	0.1	-10.0 - 10.0	cm^{-1}
I_G	0.5	0.1 - 1.0	
σ_G	12	10.0 - 15.0	cm^{-1}
Δ_G	0.1	0.1 - 1.0	cm^{-1}
σ_ν	eq. 15	0.1 - 1.0	cm^{-1}
δ_ν	0.1	-2.0 - 2.0	cm^{-1}

Table 3: Summary of the initialization and boundaries used for the calibration inversion.

The minimization step needs an initialization of these parameters to look for the best fit. The initialization is crucial for a non-convex problem (which is the case here, since the problem is non-linear), that is why we tested several cases and finally reach a good optimum using the set of parameters for the initialization described in table 3.

5. Justification of the continuum removal

All modeled effects are not able to perfectly fit both the overall shape of the spectra and the absorption lines of the observation as shown in figure 5. In this figure, we applied the calibration procedure with/without the continuum removal (Fig. 5 A and B). One can see that without the continuum removal, the fitting procedure is dominated by the large-scale feature and unfortunately not coherent with detailed solar line shape. Such results imply that in the present state of instrument knowledge, it is not possible to take into account a precise instrumental transfer function for both shape and solar lines.

In order to check the consistency, we tried an alternative approach assuming perfectly known spectral calibration (Fig. 5 C). This may not be achievable in actual data analysis and would requires another pre-processing step of spectral calibration. Results show that the reconstruction is acceptable contrarily to the case without continuum removal (Fig. 5 B). Both continuum and solar lines can be reasonably well fitted, but the best reconstruction is for the fully blind case (inversion of the spectral calibration with continuum removal) (Fig. 5 A). As one of the main advantages of LNO being its very high spectral resolution, one would emphasize the spectral line reconstruction instead of the continuum shape.

Here three strategies are possible. The first approach is to improve the characterization of the

instrument, in particular by trying to handle the temperature dependence of the AOTF and grating blaze function shape. Due to the small amount of in-flight solar data acquisition, this strategy may be difficult, in particular to distinguish temperature dependence and temporal dependence (due to the degradation of the detector in space for instance). In addition, an improvement of the instrumental characterization using a spare ground instrument always rise the question of its representativity.

A second approach would be purely empirical (on in-flight data only, no reference solar spectrum). By assuming negligible temporal variability, Thomas et al. (2021) propose a fully empirical calibration, by estimating a comprehensive transfer function (including instrumental transfer function, sensitivity, and solar spectrum) and its temperature dependence, interpolated from actual data. This strategy, based on observation only, may be biased due to the noise in the data (despite an SNR > 1000) and possible temporal variability. Nevertheless, this approach has the advantage to keep the large scale spectral features.

A third approach, proposed in the present article (see section 4.2.4), is to solve the problem by removing the continuum, focusing on small-scale spectral features, but possibly erasing large-scale spectral feature. This approach takes advantage, as previously mentioned, that the instrumental transfer function is normalized, and thus filtering would not change the level. In addition, the potential alteration of the large-scale feature would be identical for simulated and observed spectra, and thus would produce no bias, as also performed on NOMAD-SO channel (Villanueva et al., 2021; Knutsen et al., 2021).

The main advantage of such an approach is that it allows to keep the spectral radiance level (which is of primary importance for absolute photometric calibration) and produce flat continuum spectra. The validity of this approach can be measured by the root-mean-square error (RMSE) that should be low in comparison to the signal, but also by the coherence of the sensitivity measurement (consecutive measurement should be somehow similar). We propose hereafter to follow this strategy, which has the advantage to avoid any assumption of the temporal stability of the NOMAD instrument.

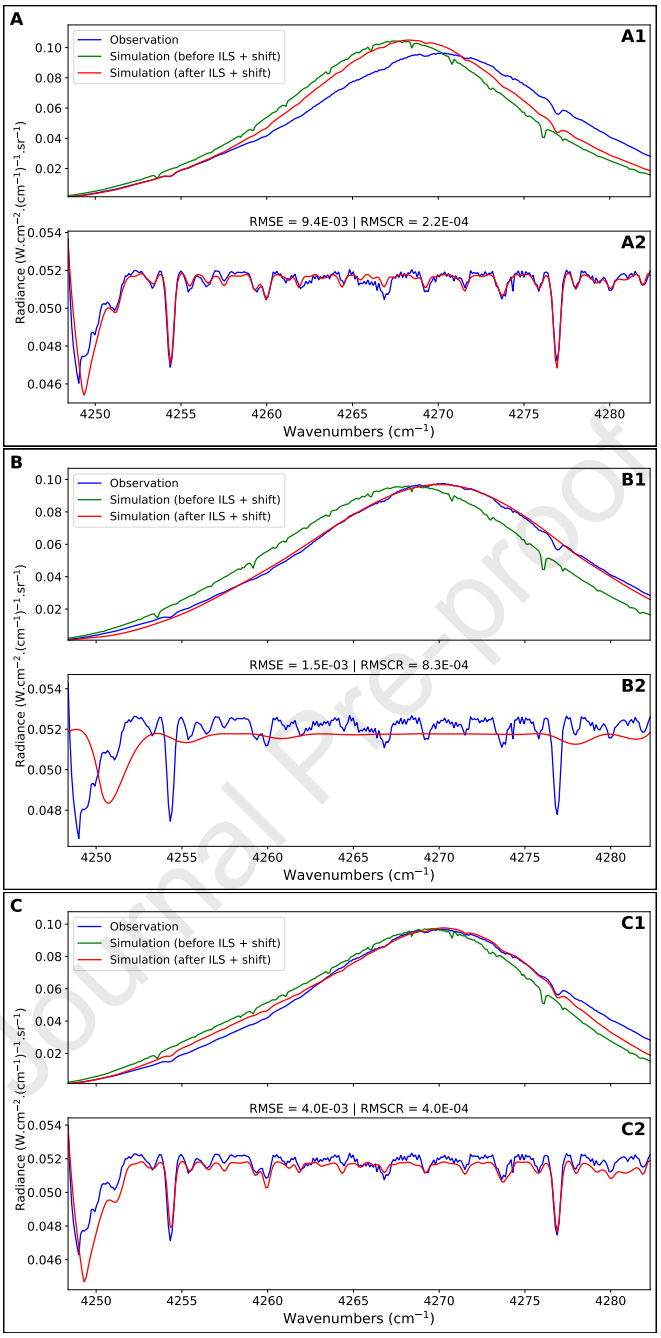

Figure 5: (A) Estimation of the inversion with continuum removal using the minimization equation 21. Note that the first 50 spectels on the left (up to 4253.5 cm^{-1}) are not included in the inversion due to low signal to noise ratio. (A1) Comparison between an observation ($S_{obs}(\nu)$, in blue) and two types of calibration inversion: before integration of the wavenumber shift and ILS ($S_{sim}^{instru}(\nu)$, in green) and after ($S_{sim}^{smooth,resamp}(\nu)$, in red). The RMSE indicates the quality of the fit. (A2) Comparison between an observation (S_{obs}^{flat}, in blue) and the simulation ($S_{sim}^{smooth,resamp,flat}(\nu)$, in red) both after continuum removal. The RMSCR (RMSE after continuum removal) indicates the quality of the fit. (B) Same as (A) without continuum removal. (C) same as (A) without continuum removal but with spectral calibration assumed to be perfectly known. For the (B2) and (C2) plots we compute the continuum removal on the results of the inversion (continuum removal was not included in the inversion).

6. Results

Fit of order 189. An interesting way to check the validity of the model is to compare observations and simulations at the spectrum scale. Figure 6 shows such comparison for order 189 on the whole of a fullscan (here 14/03/2019), as an example. Here the spectra are flat due to the continuum removal step which allows apprehending only the level of the spectrum and the position of the bands. The 13 observation sequences are shown in a shade of gray while the optimized simulation after the inversion is shown in colors. The residue between the observation and the simulation is also indicated. Both the main and weak solar lines are well reproduced and the small discrepancies are within the continuum and related to very weak solar lines. As the position and depth of the line are mainly controlled by the AOTF transfer function, with the secondary lobes of the transfer function being responsible for the leakage of adjacent orders on the central order (here 189). This contribution is expected to significantly increase the intensity of such solar lines, especially if they are located on the edges of the order, as they can be duplicated. Order 189 displays such potentiality with two main solar lines on both edges of the detector. One can see that the model perfectly accounts for this contribution since the simulation match very well the observation (relative RMS = 0.43%), no matter the observation sequence.

RMSE. Here we illustrate the overall results of the calibration model. First, the RMSE can be used for all observations as it is the quality criterion of the approach. Figure 7 shows the relative RMSE based on equation 23 for diffraction orders 110 to 200. The large majority of the points are below 1% error except for extreme orders (100-110 and 198-200) for which the SNR can be very low. We can also notice that the fullscan showing the widest dispersion is that of 01/11/2018 for which the temperature during the observation was abnormally high, leading to noisier spectra and therefore greater difficulty in obtaining a correct fit. The relative RMSE appears more dispersed for orders 150 to 190 compared to orders 120 to 150. This can be explained by the fact that high orders have stronger solar lines, which implies more information in the spectra to model the AOTF resulting in a larger standard deviation of the RMSE. However, if we exclude outliers above 1% , the average value of the relative RMSE between orders 150-190 is comparable to that of orders 120-150. This low RMSE for most of the orders (around 0.5%) tends to validate the

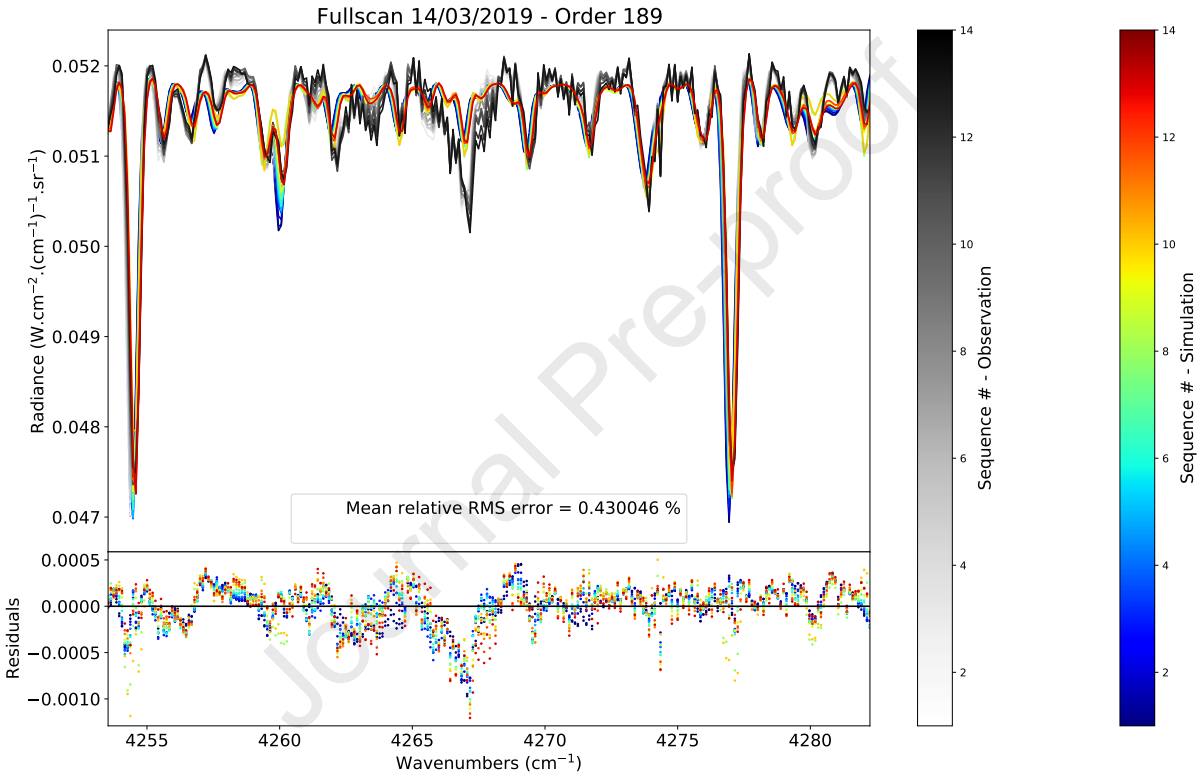

Figure 6: Fullscan of 14/03/2019, comparison between all observation sequences of order 189 (in shades of gray) and the respective optimized simulation (in colors). One can see that the main solar lines are well reproduced and the small discrepancies are only located within the continuum, near the weak solar lines. The mean relative RMS error of the 13 sequences is 0.43%.

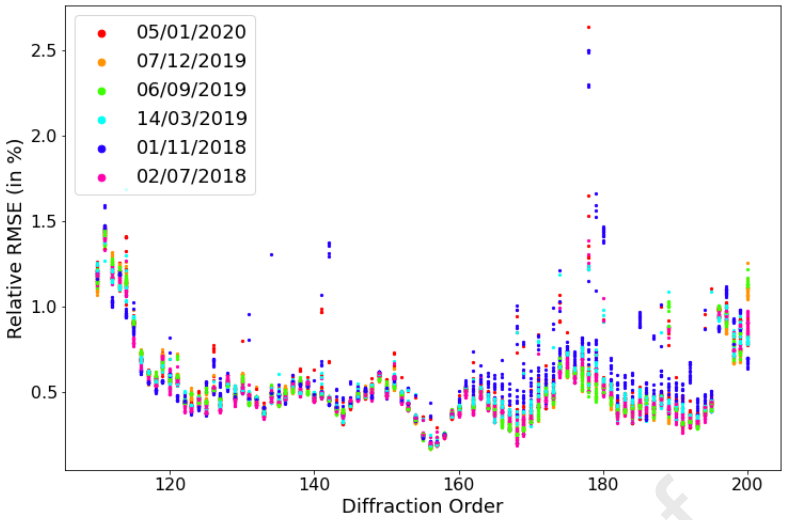

Figure 7: Relative RMS error rel_{RMSE} between the simulation and the observation for diffraction orders 110 to 200 and the 6 solar fullscans. Each point represents a single spectrum of a fullscan sequence.

spectrum-to-spectrum calibration method using a continuum removal approach.

Sensitivity. The main objective of the model is to establish the conversion factor from the measured ADU by the detector to spectral radiance. This step is done using equation 19 on all spectra of all fullscan so that we can look at the potential variations of this factor during the mission. Figure 8 shows the sensitivity curves of the LNO channel, which was estimated using equation 19. As we estimate the mean *Sensitivity* on 270 spectels, it expresses the mean radiance per counts per second of this 270 spectels. The shape of the curves is very similar to what was obtained during ground calibration before the mission: orders 120 to 135 and 165 to 190 have a higher sensitivities (Thomas, 2020). This is related to the initial design of the instrument whose purpose was a precise atmospheric characterization and these orders match the spectral range in which CO, H_2O and CH_4 have significant absorption. In addition, a drastic fall of the sensitivity near order 150 was expected and is correctly reproduced. The significant drop of the sensitivity for extreme orders illustrates well how the SNR can be low for these orders, and therefore the reasons for a higher RMSE (noisy observation are harder to fit). An exception is made for orders around 150 as the sensitivity is quite low but the RMSE of these orders is also the lowest. This is related to the fact that these orders have very few solar lines which imply an easier fit of an almost flat continuum. Nevertheless, from one fullscan to another the shape is constant but the intensity slightly changes. The first two fullscans (02/07/2018 in purple and 01/11/2011 in navy blue) display lower sensitivities while

fullscans of 06/09/2019 (in green) and 07/12/2019 (in orange) show the highest values. These differences can be explained in many ways and one of the advantages of this calibration method is to be able to test the dependence of the sensitivity such as a function of time, of the Mars-Sun distance, or the temperature. Hereafter we will demonstrate that the temperature dependence is the dominant factor.

With such variation of the instrumental sensitivity (Fig. 8), one would look if there is any correlation with other parameters. This step was made using both the nominal and redundant temperature T sensors of the LNO that monitors the temperature within the spectrometer every 2 minutes. Here we show the correlation with the nominal sensor. The temporal resolution of the temperature sensor is 2 minutes, which is too high compared to the time between two consecutive LNO observations. Temperature data were thus interpolated to match the timestamp of each fullscan. Figure 9 shows the sensitivity as a function of the temperature. Here all diffraction orders of the six fullscans are shown along with the linear regression (dotted line). The gap between the points illustrates the temperature variation between the fullscans. Within one sequence, one can see a slope that seems to be consistent between all orders showing that sensitivity decline when temperature increases. Looking at all sequences together, the relationship seems linear and we fit a line for each diffraction order:

$$Sensitivity = a.T + b \tag{24}$$

With T the temperature. The adjusted a and b values are available in public archive[1]. By postulating that the temperature is mainly responsible for the sensitivity change of the detector, and correcting these variations with a linear fit we can show that there is no sign of a correlation with time (aging of the detector) in the instrumental response of the detector (see figure 10) which was not obvious in the first place.

Regarding the absolute uncertainty of the sensitivity retrieved here, and hence on the radiance derived from the calibration. All the steps introduced in the calibration pipeline (ILS, spectral shift, AOTF parameters and continuum correction) respect the energy conservation. Thus, ac-

[1] https://doi.org/10.14768/2d7688ba-2e5f-473c-8e03-763e93f4bd6b

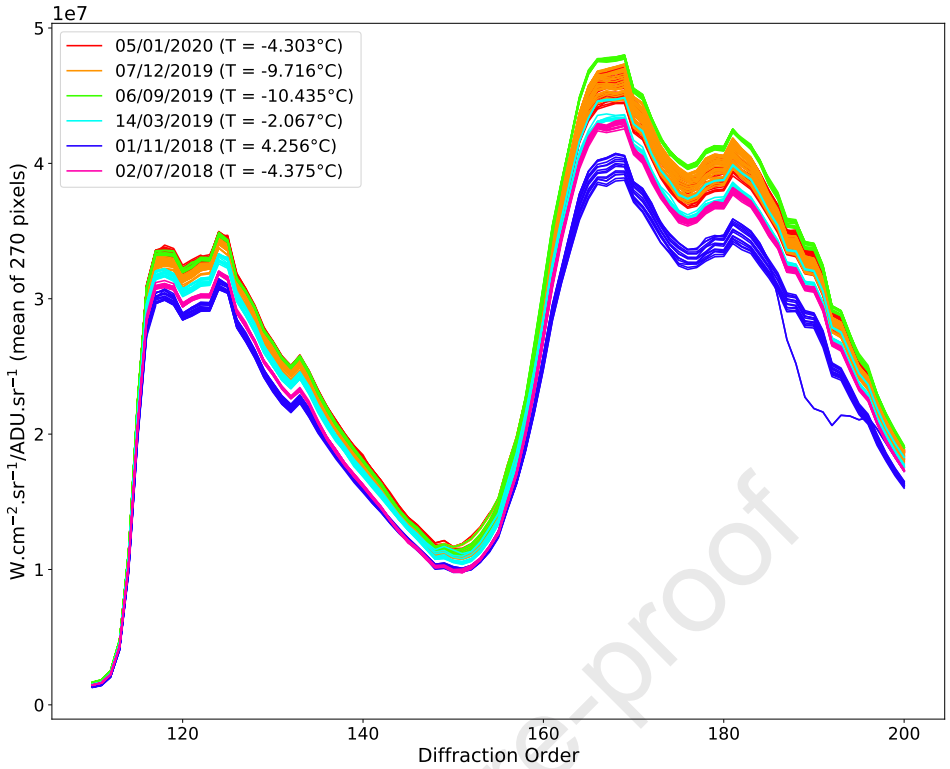

Figure 8: Radiance to counts conversion (*Sensitivity*) for diffraction orders 110 to 200 retrieved for the 6 LNO solar fullscan using equation 19. The mean temperature during the fullscan is indicated. This illustrates the sensitivity curves of the LNO channel. The shape is very consistent from one sequence to another but also between the fullscans, with two main peaks of sensitivity around orders 125 and 170 and a lower sensitivity for the extreme orders and around orders 150.

cording to equation 19, the main source of uncertainty come from the number of counts (S_{obs}^{flat} in $ADU.(cm^{-1})^{-1}.s^{-1}$) of the LNO observation of the sun and from the synthetic solar spectrum ($S_{sim}^{mooth,resamp,flat}$ in spectral radiance). The LNO observation are normalized according to equation 1 and we can assume that the uncertainty on the integration time, number of accumulation, spectral resolution and binning factor is negligible. According to Thomas et al. (2021), a typical LNO spectrum of 3000 ±500 counts would have an SNR of about 25 ±5, which gives an absolute error between 0.6% and 1%. Also, the maximum expected systematic error is 4% (Thomas et al., 2021). The uncertainty on $S_{sim}^{mooth,resamp,flat}$ is related to the initial solar spectrum, according to Chance and Kurucz (2010), the absolute accuracy of the solar spectrum is of 3.5-4%. This leads to a maximum absolute uncertainty on the radiance less than 10%. Although the maximum error may be high, the systematic error of LNO is not often expected to be 4%.

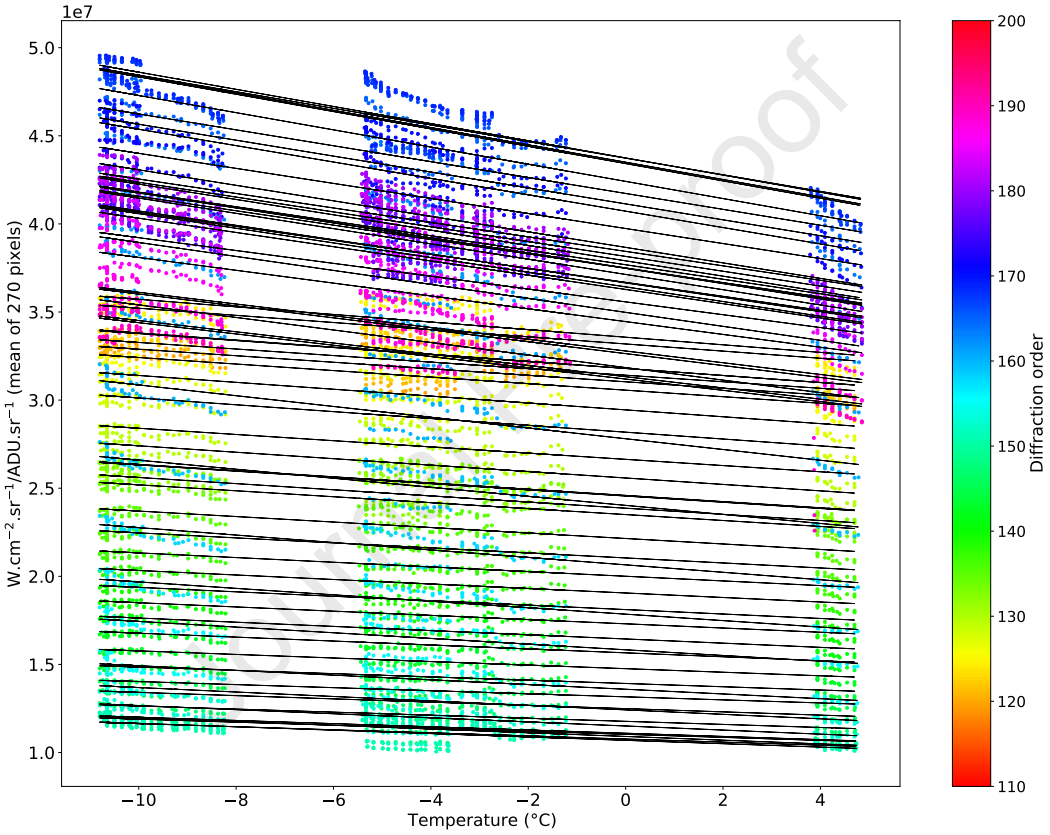

Figure 9: Sensitivity as a function of the instrumental temperature (nominal sensor). The colors refer to diffraction order and the dotted line shows the linear regression per order.

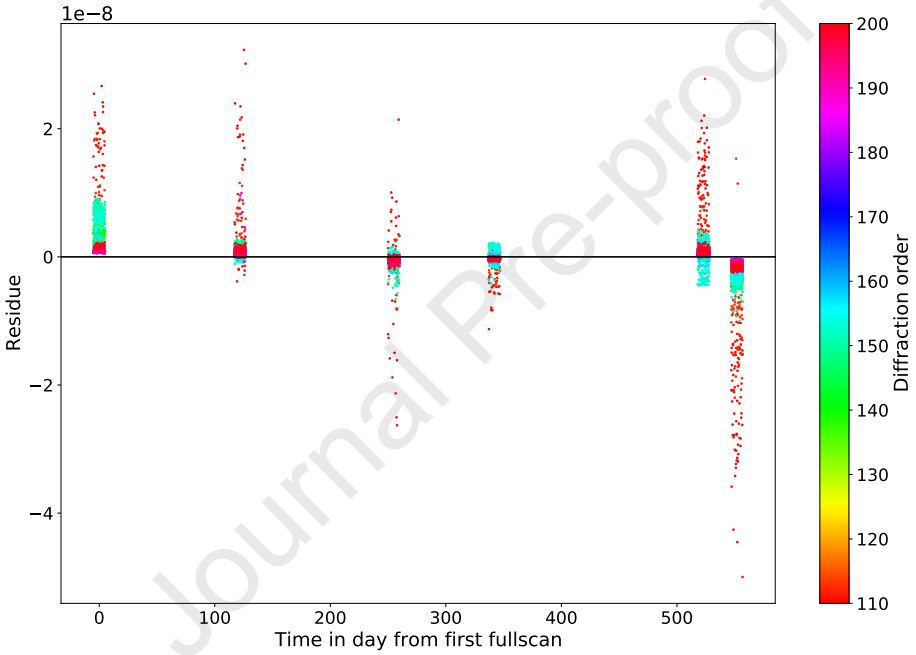

Figure 10: Residue after temperature correction of the sensitivity using eq. 24 as a function of time (in day) from first fullscan. The results are artificially spread horizontally for clarity. Despite few outliers near order 110 (in red) for which the sensitivity is very low, the residues indicate that there is no correlation of the sensitivity with time and therefore no aging of the detector to the first order.

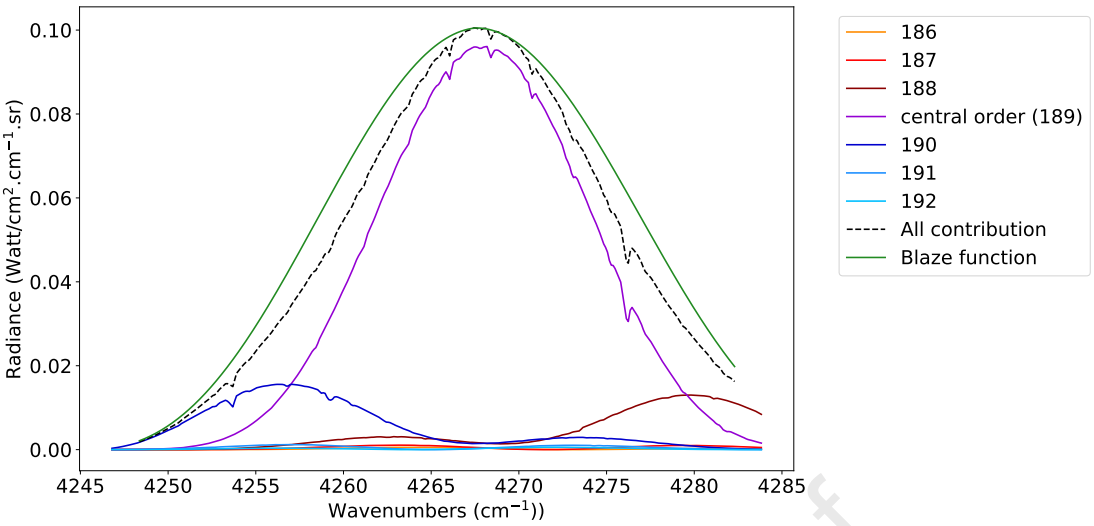

Figure 11: AOTF transfer function: contribution from the main order (189 in purple) and 3 adjacents orders. The sum of all contributions that define the final spectrum is shown in black dashed line and the Blaze function of the central order is shown in green. The main lobe of the AOTF transfer function accounts for the contribution of the central order while the sidelobes control the shape and intensity of adjacent orders which are summed onto the wavenumbers of the central order. The shape of the final spectrum is therefore constrained by the product of the Blaze function and the AOTF transfer function.

AOTF. Among all the inverted parameters six of them account for the AOTF transfer function shape. They are crucial because they account for the contribution of the main and adjacent orders which define the intensity of solar lines. An example of the transfer function retrieved after the inversion is given in figure 11 for one observation of order 189. In this case, the estimated AOTF transfer function is slightly asymmetrical, promoting a higher contribution of order 190 compared to order 188. The "bell" shape of an LNO spectrum is partly controlled by the blaze function but the AOTF sidelobes are also affecting the spectra by widening or shrinking the flanks of the continuum. To reproduce all the potential shapes of an LNO spectrum, which vary from one order to another it is necessary to integrate variations in intensity, width and offsets of the AOTF transfer function.

In the example shown figure 11 the AOTF inverted parameters to reconstruct the final spectrum are:

- $I_0 = 0.74 \pm 0.3$
- $fwhm = 17.41$ cm^{-1} ± 0.86
- $\Delta_\nu = 2.34$ cm^{-1} ± 0.53

- $I_G = 0.71 \pm 0.57$
- $\sigma_G = 12.86\ \mathrm{cm}^{-1} \pm 0.77$
- $\Delta_G = 2.33\ \mathrm{cm}^{-1} \pm 0.59$

We tested several temperature and temporal dependence and did not find any obvious correlation. These parameters define the shape of the AOTF and can therefore be strongly correlated together. This is particularly noticeable on the spectral shift of the sinc-square (Δ_ν) and the gaussian (Δ_G) whose values and uncertainties are similar. A shift of one can thus be compensated by the other, but the best fit is estimated for a similar offset of the two. This observation is the same for the intensities of the two filters (I_0 and I_G) whose uncertainties are relatively large. However, the width of the filters ($fwhm$ and σ_G) is well constrained and the values obtained are similar to what is obtained by Liuzzi et al. (2019).

Spectral calibration and ILS. Figure 12 shows the actual spectral resolution of the instrument σ_ν retrieved by the algorithm for all available data as a function of the diffraction order. A comparison with the theoretical spectral resolution computed using eq. 15 is provided. We found that σ_ν is slightly higher (mostly around 0.05) than expected but still follows the theoretical trend. Some points are way off the trend and are often related to orders with lower sensitivity and thus more noise, so the convolution requires a much wider ILS to get a proper fit. This is illustrated with the fullscan of 01/11/2018 (navy blue points), which corresponds to the highest temperature and lowest sensitivity (see fig. 9, navy blue curves)

The wavenumber shift δ_ν account for potential deviation from the theoretical spectral calibration (see eq. 4). Figure 13 (top panel) shows the retrieved shift as a function of the diffraction order for the 6 fullscans. When expressed in pixel, the shift appears constant with the diffraction order. Nevertheless, the shifting intensity is different from one fullscan to another. We tested a temperature dependence of the wavenumber shift δ_ν in figure 13 (bottom panel) using orders 130 to 190 and found a slope of about 0.75 pixels per degree which is consistent with what Liuzzi et al. (2019) and Thomas et al. (2021) reported with values of 0.71 and 0.83 pixels per degree.

The wavenumber shift and ILS analysis emphasize that our approach works well for diffraction

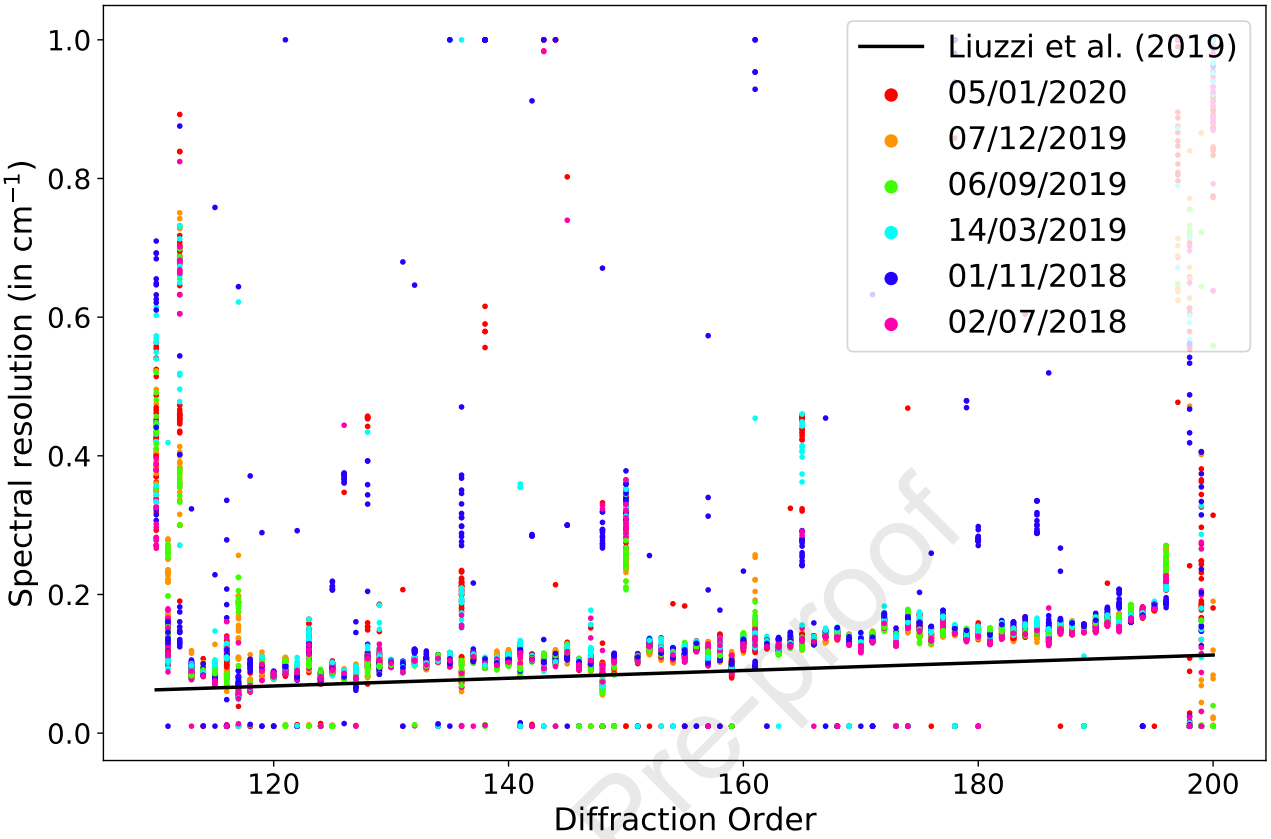

Figure 12: Actual ILS spectral resolution σ_ν retrieved from the calibration inversion. Each point corresponds to a single spectrum, the color refers to the 6 fullscans used. The empirical spectral resolution computed using eq. 15 (Liuzzi et al., 2019)) is shown as a black line. For a clearer comparison, data from Liuzzi et al. (2019) were converted from a Gaussian FWHM to a Gaussian standard deviation considering $FWHM = 2\sqrt{2\ln 2}\sigma$

orders with multiple well-defined solar lines because the continuum removal approach allows assigning a greater weight to the variations brought by the solar lines and therefore to the AOTF parameters. The quality of the fit is higher for orders with the number of strong solar lines. Also, such orders have often higher sensitivities which promote a better estimation of the wavenumber shift and the spectral resolution.

7. Calibration pipeline

With such an approach any nadir observation can be calibrated to spectral radiance, the pipeline to calibrate a raw nadir spectrum is as follows: first, the raw spectrum is normalized following equation 1 with the spectral resolution (eq. 15). Second, we remove the continuum using eq. 18 to get a flat spectrum. Then, knowing the temperature at the time of the measurement from housekeeping and using coefficients a and b from eq. 24, we apply the sensitivity factor to convert

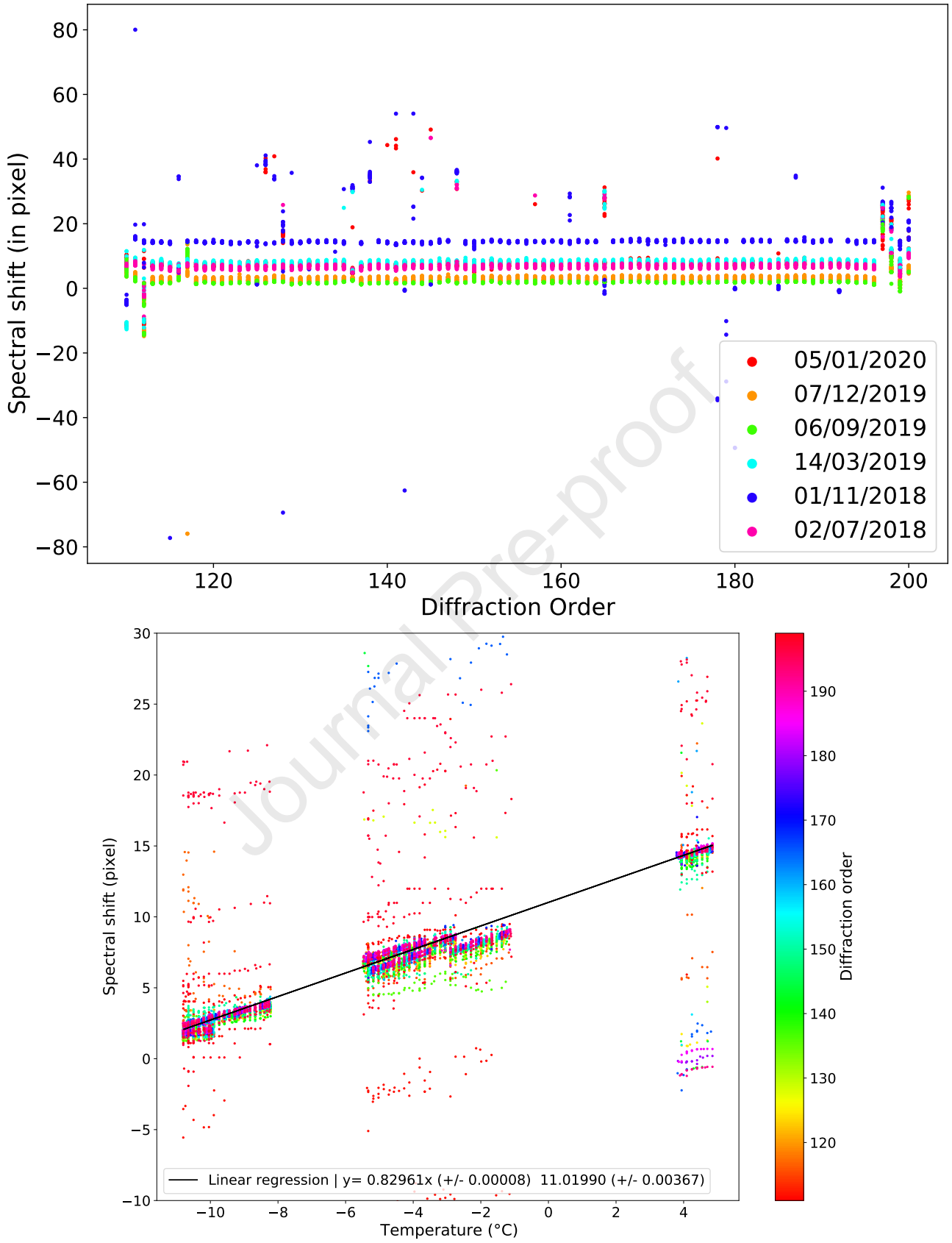

Figure 13: Wavenumber shift δ_ν (in pixel units) retrieved from the calibration inversion. Top image show the spectal shift as a function of the diffraction order, colors refer to the fullscan. Bottom image shows the shift as a function of temperature. The color refers to the diffraction order.

the normalized ADU to spectral radiance (see Eq. 20). This product can be used to create reflectance map such as the one reported in Thomas et al. (2021) applying the following equation:

$$R = \pi . \frac{I}{F} \tag{25}$$

With I the spectral radiance and $F = S_L.\pi.\cos(\theta_i)$ the spectral irradiance received by the surface (see section 3.2) accounting for the incident angle θ_i and the distance of the sun at the time of the observation. A typical reflectance map obtained via our approach is shown in figure 14 for order 189 using data spread over mostly 3 years. A comparison with the reflectance obtained following the method of Thomas et al. (2021) is also shown (fig. 14, bottom panel). The two calibrations provide very similar results with a linear coefficient of 1.024 and -0.017 (correlation coefficient of 0.987) despite different approaches. This result shows that both calibrations are in agreement mostly within 3% and that our approach underestimates (resp. overestimates) the one from Thomas et al., 2011 for reflectance < 0.2 (resp. > 0.2).

8. Conclusion

We propose an alternative calibration method for the LNO data using reference solar spectra with the advantage of being able to investigate the correlations between the instrumental sensitivity and the temperature of the instrument. By having done this, we can understand the potential temporal variations of the instrument due to its aging. The method is based on the adjustment of a synthetic spectrum to the solar data acquired with NOMAD-LNO fullscan operation mode, which allows a calibration over the whole spectral range of the instrument (different orders), using an analytical model that simulate the instrumental effects. To realize this calibration, we propose to focus on the level and the fine solar bands shape and remove the continuum. This strategy allows to correct of unknowns in the instrumental AOTF/blaze functions but could possibly remove the large spectral feature of the order. However, by performing the same continuum removal to the synthetic data, it is possible to compare synthetic and observation data without bias (Villanueva et al., 2021; Knutsen et al., 2021).

In addition, this method makes it possible to test the correlations between sensitivity and instrumental parameters (AOTF shape, ILS, wavenumber shift), such as temperature and time.

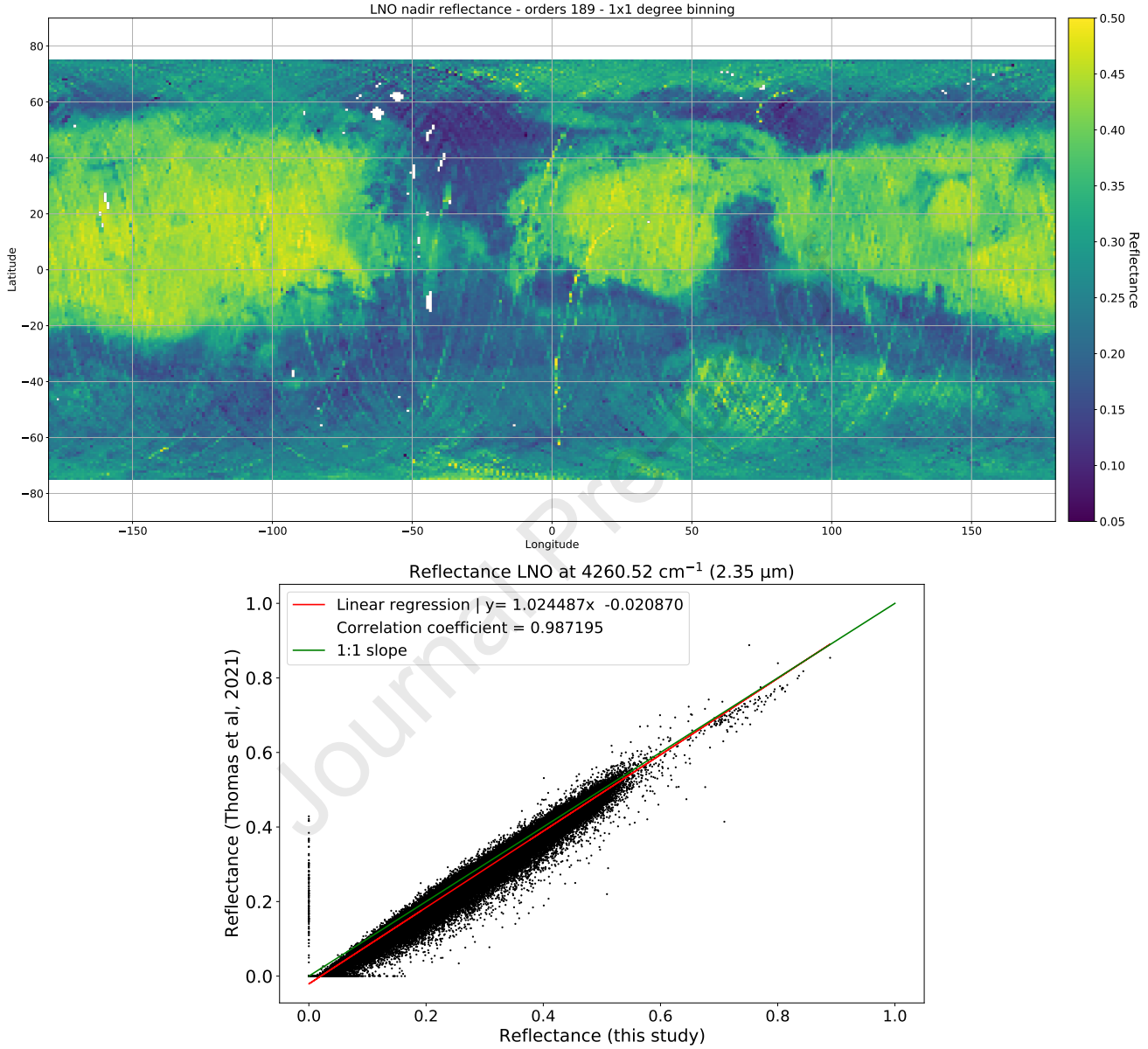

Figure 14: Reflectance of order 189 at 4260.52 cm^{-1} using 1230 orbits from 29/03/2018 to 19/10/2021. Data with incident angle higher than 80° were removed to promote a better SNR. Also, to reduce albedo variation due to seasonal effects at high latitude we only considered data between latitude 75° N and 75° S. The top image shows a map binned onto a 1°x1° grid using 134,738 spectra. Bottom shows a comparison between the reflectance estimate in this study and the reflectance obtained using the approach of Thomas et al. (2021) for the same order.

By doing this, we show that there is at first degree a linear relationship between the temperature and the sensitivity. By removing this effect, we demonstrated that there is no sign of temporal change in the sensitivity, which validates the calibration method proposed by Thomas et al. (2021). If any temporal variations of the detector occur in the future, our method should be able to capture them.

Finally, with such a model, one can calibrate any nadir observation to spectral radiance and reflectance data. The calibrated data show a very strong correlation with the approach proposed by Thomas et al. (2021) mostly within 3%. The two approaches are therefore complementary and coherent.

Acknowledgements. The NOMAD experiment is led by the Royal Belgian Institute for Space Aeronomy (IASB-BIRA), assisted by Co-PI teams from Spain (IAA-CSIC), Italy (INAF-IAPS), and the United Kingdom (Open University). We would like to thank everyone involved in the ExoMars project. Funding: This project acknowledges funding by the Belgian Science Policy Office (BELSPO), with the financial and contractual coordination by the ESA Prodex Office (PEA 4000103401, 4000121493), by Spanish Ministry of Science and Innovation (MCIU) and by European funds under grants PGC2018-101836-B-I00 and ESP2017-87143-R (MINECO/FEDER), as well as by UK Space Agency through grants ST/V002295/1, ST/V005332/1 and ST/S00145X/1 and Italian Space Agency through grant 2018-2-HH.0. This work was supported by the Belgian Fonds de la Recherche Scientifique – FNRS under grant number 30442502 (ET_HOME). The IAA/CSIC team acknowledges financial support from the State Agency for Research of the Spanish MCIU through the "Center of Excellence Severo Ochoa" award for the Instituto de AstrofÃsica de AndalucÃa (SEV-2017-0709). US investigators were supported by the National Aeronautics and Space Administration. Canadian investigators were supported by the Canadian Space Agency. We acknowledge support from the "Institut National des Sciences de l'Univers" (INSU), the "Centre National de la Recherche Scientifique" (CNRS) and "Centre National d'Etudes Spatiales" (CNES) through the "Programme National de Planétologie". This work is partly funded through the ESA co-funded PhD studentships programme (idea: I-2019-01294).

Byrd, R.H., Lu, P., Nocedal, J., Zhu, C., 1995. A limited memory algorithm for bound constrained optimization. SIAM Journal on Scientific Computing 16, 1190–1208. doi:10.1137/0916069.

Chance, K., Kurucz, R., 2010. An improved high-resolution solar reference spectrum for earth's atmosphere measurements in the ultraviolet and visible and and near infrared. Journal of Quantitative Spectroscopy and Radiative Transfer 111, 1289–1295. doi:10.1016/j.jqsrt.2010.01.036.

Eilers, Paul, Boelens, Hans, 2005. Baseline corection with asymmetric least squares smoothing.

Hase, F., Wallace, L., McLeod, S.D., Harrison, J.J., Bernath, P.F., 2010. The ACE-FTS atlas of the infrared solar spectrum. Journal of Quantitative Spectroscopy and Radiative Transfer 111, 521–528. doi:10.1016/j.jqsrt.2009.10.020.

Knutsen, E.W., Villanueva, G.L., Liuzzi, G., Crismani, M.M., Mumma, M.J., Smith, M.D., Vandaele, A.C., Aoki, S., Thomas, I.R., Daerden, F., Viscardy, S., Erwin, J.T., Trompet, L., Neary, L., Ristic, B., Lopez-Valverde, M.A., Lopez-Moreno, J.J., Patel, M.R., Karatekin, O., Bellucci, G., 2021. Comprehensive investigation of mars methane and organics with ExoMars/NOMAD. Icarus 357, 114266. doi:10.1016/j.icarus.2020.114266.

Liuzzi, G., Villanueva, G.L., Mumma, M.J., Smith, M.D., Daerden, F., Ristic, B., Thomas, I., Vandaele, A.C., Patel, M.R., Lopez-Moreno, J.J., Bellucci, G., 2019. Methane on mars: New insights into the sensitivity of CH4 with the NOMAD/ExoMars spectrometer through its first in-flight calibration. Icarus 321, 671–690. doi:10.1016/j.icarus.2018.09.021.

Marquardt, E., Le, J., Radebaugh, R., 2000. Cryogenic material properties database. 11th International Cryocooler Conference .

Neefs, E., Vandaele, A.C., Drummond, R., Thomas, I.R., Berkenbosch, S., Clairquin, R., Delanoye, S., Ristic, B., Maes, J., Bonnewijn, S., Pieck, G., Equeter, E., Depiesse, C., Daerden, F., Ransbeeck, E.V., Nevejans, D., Rodriguez-Gómez, J., López-Moreno, J.J., Sanz, R., Morales, R., Candini, G.P., Pastor-Morales, M.C., del Moral, B.A., Jeronimo-Zafra, J.M., Gómez-López, J.M., Alonso-Rodrigo, G., Pérez-Grande, I., Cubas, J., Gomez-Sanjuan, A.M., Navarro-Medina, F., Thibert, T., Patel, M.R., Bellucci, G., Vos, L.D., Lesschaeve, S., Vooren, N.V., Moelans, W.,

Aballea, L., Glorieux, S., Baeke, A., Kendall, D., Neef, J.D., Soenen, A., Puech, P.Y., Ward, J., Jamoye, J.F., Diez, D., Vicario-Arroyo, A., Jankowski, M., 2015. NOMAD spectrometer on the ExoMars trace gas orbiter mission: part 1—design and manufacturing and testing of the infrared channels. Applied Optics 54, 8494. doi:10.1364/ao.54.008494.

Nevejans, D., Neefs, E., Ransbeeck, E.V., Berkenbosch, S., Clairquin, R., Vos, L.D., Moelans, W., Glorieux, S., Baeke, A., Korablev, O., Vinogradov, I., Kalinnikov, Y., Bach, B., Dubois, J.P., Villard, E., 2006. Compact high-resolution spaceborne echelle grating spectrometer with acousto-optical tunable filter based order sorting for the infrared domain from 2.2 to 4.3 μm. Applied Optics 45, 5191. doi:10.1364/ao.45.005191.

Smith, M., 2021. Nomad nadir-geometry retrievals of co in the mars atmosphere. doi:10.17632/PX89DK6CK9.1.

Thomas, I., 2020. Nomad experiment to archive interface control document. URL: ftp://npsa01.esac.esa.int/pub/mirror/ExoMars2016/em16_tgo_nmd/document/EAICDhttps://nomad.aeronomie.be/ProjectDir/data/nomad_hdf5_datasets.pdf.

Thomas, I., Aoki, S., Trompet, L., Robert, S., Depiesse, C., Willame, Y., Cruz-Mermy, G., Schmidt, F., Erwin, J., Vandaele, A., Daerden, F., Mahieux, A., Neefs, E., Ristic, B., Hetey, L., Patel, M., Moreno, J.L., Bellucci, G., , the NOMAD Team, 2021. Calibration of nomad onboard the exomars trace gas orbiter: Part 2 - the lno channel. Submitted .

Thomas, I.R., Vandaele, A., Robert, S., Neefs, E., Drummond, R., Daerden, F., Delanoye, S., Ristic, B., Berkenbosch, S., Clairquin, R., Maes, J., Bonnewijn, S., Depiesse, C., Mahieux, A., Trompet, L., Neary, L., Willame, Y., Wilquet, V., Nevejans, D., Aballea, L., Moelans, W., Vos, L.D., Lesschaeve, S., Vooren, N.V., Lopez-Moreno, J.J., Patel, M.R., Bellucci, G., the NOMAD Team, 2016. Optical and radiometric models of the NOMAD instrument part II: the infrared channels - SO and LNO. Optics Express 24, 3790. doi:10.1364/oe.24.003790.

Vago, J., Witasse, O., Svedhem, H., Baglioni, P., Haldemann, A., Gianfiglio, G., Blancquaert, T.,

McCoy, D., de Groot, R., 2015. ESA ExoMars program: The next step in exploring mars. Solar System Research 49, 518–528. doi:10.1134/s0038094615070199.

Vandaele, A., Neefs, E., Drummond, R., Thomas, I., Daerden, F., Lopez-Moreno, J.J., Rodriguez, J., Patel, M., Bellucci, G., Allen, M., Altieri, F., Bolsée, D., Clancy, T., Delanoye, S., Depiesse, C., Cloutis, E., Fedorova, A., Formisano, V., Funke, B., Fussen, D., Geminale, A., Gérard, J.C., Giuranna, M., Ignatiev, N., Kaminski, J., Karatekin, O., Lefèvre, F., López-Puertas, M., López-Valverde, M., Mahieux, A., McConnell, J., Mumma, M., Neary, L., Renotte, E., Ristic, B., Robert, S., Smith, M., Trokhimovsky, S., Auwera, J.V., Villanueva, G., Whiteway, J., Wilquet, V., Wolff, M., 2015. Science objectives and performances of NOMAD and a spectrometer suite for the ExoMars TGO mission. Planetary and Space Science 119, 233–249. doi:10.1016/j.pss.2015.10.003.

Vandaele, A.C., , Korablev, O., Daerden, F., Aoki, S., Thomas, I.R., Altieri, F., López-Valverde, M., Villanueva, G., Liuzzi, G., Smith, M.D., Erwin, J.T., Trompet, L., Fedorova, A.A., Montmessin, F., Trokhimovskiy, A., Belyaev, D.A., Ignatiev, N.I., Luginin, M., Olsen, K.S., Baggio, L., Alday, J., Bertaux, J.L., Betsis, D., Bolsée, D., Clancy, R.T., Cloutis, E., Depiesse, C., Funke, B., Garcia-Comas, M., Gérard, J.C., Giuranna, M., Gonzalez-Galindo, F., Grigoriev, A.V., Ivanov, Y.S., Kaminski, J., Karatekin, O., Lefèvre, F., Lewis, S., López-Puertas, M., Mahieux, A., Maslov, I., Mason, J., Mumma, M.J., Neary, L., Neefs, E., Patrakeev, A., Patsaev, D., Ristic, B., Robert, S., Schmidt, F., Shakun, A., Teanby, N.A., Viscardy, S., Willame, Y., Whiteway, J., Wilquet, V., Wolff, M.J., Bellucci, G., Patel, M.R., López-Moreno, J.J., Forget, F., Wilson, C.F., Svedhem, H., Vago, J.L., and, D.R., 2019. Martian dust storm impact on atmospheric h2o and d/h observed by ExoMars trace gas orbiter. Nature 568, 521–525. doi:10.1038/s41586-019-1097-3.

Vandaele, A.C., , Lopez-Moreno, J.J., Patel, M.R., Bellucci, G., Daerden, F., Ristic, B., Robert, S., Thomas, I.R., Wilquet, V., Allen, M., Alonso-Rodrigo, G., Altieri, F., Aoki, S., Bolsée, D., Clancy, T., Cloutis, E., Depiesse, C., Drummond, R., Fedorova, A., Formisano, V., Funke, B., González-Galindo, F., Geminale, A., Gérard, J.C., Giuranna, M., Hetey, L., Ignatiev, N.,

Kaminski, J., Karatekin, O., Kasaba, Y., Leese, M., Lefèvre, F., Lewis, S.R., López-Puertas, M., López-Valverde, M., Mahieux, A., Mason, J., McConnell, J., Mumma, M., Neary, L., Neefs, E., Renotte, E., Rodriguez-Gomez, J., Sindoni, G., Smith, M., Stiepen, A., Trokhimovsky, A., Auwera, J.V., Villanueva, G., Viscardy, S., Whiteway, J., Willame, Y., Wolff, M., 2018. NOMAD and an integrated suite of three spectrometers for the ExoMars trace gas mission: Technical description and science objectives and expected performance. Space Science Reviews 214. doi:10.1007/s11214-018-0517-2.

Vandaele, A.C., Mahieux, A., Robert, S., Berkenbosch, S., Clairquin, R., Drummond, R., Letocart, V., Neefs, E., Ristic, B., Wilquet, V., Colomer, F., Belyaev, D., Bertaux, J.L., 2013. Improved calibration of SOIR/venus express spectra. Optics Express 21, 21148. doi:10.1364/oe.21.021148.

Villanueva, G.L., Liuzzi, G., Crismani, M.M.J., Aoki, S., Vandaele, A.C., Daerden, F., Smith, M.D., Mumma, M.J., Knutsen, E.W., Neary, L., Viscardy, S., Thomas, I.R., Lopez-Valverde, M.A., Ristic, B., Patel, M.R., Holmes, J.A., Bellucci, G., and, J.J.L.M., 2021. Water heavily fractionated as it ascends on mars as revealed by ExoMars/NOMAD. Science Advances 7, eabc8843. doi:10.1126/sciadv.abc8843.

Zhu, C., Byrd, R.H., Lu, P., Nocedal, J., 1997. Algorithm 778: L-BFGS-b: Fortran subroutines for large-scale bound-constrained optimization. ACM Transactions on Mathematical Software 23, 550–560. doi:10.1145/279232.279236.

Highlights

The LNO channel is 1 of 3 spectrometers in NOMAD on ExoMars Trace Gas Orbiter.
The LNO channel observes Mars in limb, nadir and solar occultation modes
This article describes an alternative method of calibration for the LNO channel data based on a comparison between observation of the sun by the LNO channel and a synthetic solar spectrum
Temperature and time dependence of the instrumental responsivity were tested.
Nadir observations can be calibrated radiometrically

Author Statement

Guillaume. Cruz Mermy : Methodology, Investigation, Software, Validation, Writing
Frédéric Schmidt : Methodology, Investigation, Software, Validation, Supervision
Ian R. Thomas : Investigation, Software, Validation, Supervision
Frank Daerden : Validation, Supervision
Bojan Ristic : Validation, Supervision
Manish R. Patel : Validation, Supervision
Jose Juan Lopez-Moreno : Validation, Supervision
Giancarlo Belluci : Validation, Supervision
Ann Carine Vandaele : Validation, Supervision

Declaration of interests

☒ The authors declare that they have no known competing financial interests or personal relationships that could have appeared to influence the work reported in this paper.

☐The authors declare the following financial interests/personal relationships which may be considered as potential competing interests: